Tracking Myocardial Deformation Using Phase Contrast MR Velocity Fields: A Stochastic Approach

François G. Meyer, *Member, IEEE,*, R. Todd Constable, *Member, IEEE,*, Albert J. Sinusas, and James. S. Duncan, *Senior Member, IEEE,*

Abstract— **In this paper, we propose a new approach for tracking the deformation of the Left Ventricular (LV) myocardium from two-dimensional Magnetic Resonance (MR) phase contrast velocity fields. The use of phase contrast MR velocity data in cardiac motion problems has been introduced by others [1] and shown to be potentially useful for tracking discrete tissue elements, and therefore characterizing LV motion. However, we show here that these velocity data i.) are extremely noisy near the LV borders and ii.) cannot alone be used to estimate the motion and the deformation of the entire myocardium due to noise in the velocity fields. In this new approach, we use the natural spatial constraints of the endocardial and epicardial contours, detected semi-automatically in each image frame, to help remove noisy velocity vectors at the LV contours. The information from both the boundaries and the phase contrast velocity data is then integrated into a deforming mesh that is placed over the myocardium at one time frame and then tracked over the entire cardiac cycle. The deformation is guided by a Kalman filter that provides a compromise between a.) believing the dense field velocity and the contour data when it is crisp and coherent in a local spatial and temporal sense and b.) employing a temporally smooth cyclic model of cardiac motion when contour and velocity data are not trustworthy. The Kalman filter is particularly well suited to this task as it produces an optimal estimate of the LV's kinematics (in the sense that the error is statistically minimized) given incomplete and noise corrupted data, and given a basic dynamical model of the LV. The method has been evaluated with simulated data ; the average error between tracked nodes and theoretical position was 1.8% of the total path length. The algorithm has also been evaluated with phantom data ; the average error was 4.4% of the total path length. We show that in our initial tests with phantoms that the new approach shows small, but concrete improvements over previous techniques that used primarily phase contrast velocity data alone. We feel that these improvements will be amplified greatly as we move to direct comparisons in** ***in vivo*** **and three-dimensional datasets.**

Keywords—: **tracking, nonrigid motion, velocity fields, phase contrast MRI, left ventricular motion**

Manuscript received January 18, 1995; revised April 22, 1996. This work was supported in part by the National Heart, Lung, and Blood Institute under NIH Grant R01HL44803; by United States Air Force under Grant F49620-93-1-0575; and by the Whitaker Foundation. The associate editor responsible for coordinating the review of this paper and recommending its publication was E.R. McVeigh.

François G. Meyer is with the Departments of Mathematics and Diagnostic Radiology, Yale University, New Haven, CT 06510, USA, e-mail: `francois.meyer@yale.edu`

R. Todd Constable is with the Department of Diagnostic Radiology, Yale University, New Haven, CT 06510, USA

Albert J. Sinusas is with the Departments of Medicine and Diagnostic Radiology, Yale University, New Haven, CT 06510, USA

James. S. Duncan is with the Departments of Diagnostic Radiology and Electrical Engineering, Yale University, New Haven, CT 06510, USA

I. Introduction

Many cardiac disorders manifest as abnormalities of myocardial function. Noninvasive measurements of the regional contractility and myocardial function are thus of importance. In order to analyze and quantify the deformation of tissue elements inside the myocardium, we need to follow these segments of myocardium throughout the cardiac cycle. The ability to accurately track the same region of interest is thus critical. A large body of work has been performed on the problem of tracking rigid and non rigid objects from a sequence of images. The many different methods can be classified into two broad groups.

1) Correspondence Approach. The first class is comprised of methods that exploit the correspondence between distinct features over time. Each of these methods is based on three stages. Usually the first stage requires the extraction of material landmarks or point features. These features can be points of highest curvature [2], [3], [4] in the case of certain types of nonrigid motion. A more accurate approach to finding landmarks might be by using implanted beads in the myocardium, which has provided clinical information about regional myocardial strain [5]. However the use of these invasive markers is limited. Alternatively, tissue tagging with MRI makes it possible to embed in the image a large number of material landmarks [6], [7], [8], [9], [10], [11]. These non invasive landmarks move along with the tissue.

During the second stage the correspondence between landmarks is established over time. The correspondence can be achieved manually [10], or using automatic procedures that exploit the spatial organization of the landmarks [8], or the continuity of motion.

Finally, the last stage consists of recovering the motion of the object from the sparse set of landmarks' trajectories. Unfortunately, without further information, the problem is underconstrained. The landmarks' trajectories provide only a sparse sampling of the spatiotemporal trajectory of the object. If the spatiotemporal trajectory is smooth enough, then the sampling provided by the landmarks may be sufficient to recover a unique trajectory. This leads typically therefore to a classic assumption of the smoothness of motion. Pentland [12] assumes that the motion of the object can be characterized by low order modes of deformations. Young and Axel [13], [14] use a global smoothing technique, where the rate of change of the deformation gradient tensor is minimized. Alternatively, a parametric model of the object may be available and makes it possible to constrain the unknown spatiotemporal trajectory of the object [15].

2) Velocity Fields Approach. The second class of methods contains techniques that exploit time sequences of velocity fields. These methods rely on two stages. First the instantaneous velocity is estimated everywhere inside the object of interest. The velocity can be estimated from the spatiotemporal variation of the intensity function [16], [9], [17], or it can be directly calculated from the imaging technique [18], [19], [1].

The second stage is the motion recovery from the temporal sequence of snapshots of the velocity fields. The difficulty arise from the fact that Eulerian (or spatial) velocity fields are measured with a large time step, and we want to recover the Lagrangian path of each point in the object. In principle the integration of the Eulerian velocity should yield the path of each material point. In practice serious numerical difficulties arise. At a given instant the estimated position may not correspond to the true position of the material point. Therefore the velocity at this location will not coincide with the true velocity. If we integrate this velocity in order to estimate the position at the next instant, then errors in the position will amplify. This means that numerical errors in positions can grow rapidly in time as numerical integration proceeds. In addition the time step between two velocity fields is not controllable, and the integration can yield inaccurate results when the object is undergoing a large acceleration. Another related problem stems from the fact that the velocity is only given on a discrete grid with limited resolution. Interpolation schemes are required to estimate velocities at positions not on the grid [20]. Finally any noise in the velocity will be transmitted to the position estimates. These errors may also accumulate over time. The authors in [19], [21], [22] have encountered these difficulties when tracking pixels, or clusters of pixels in the myocardium using phase contrast MRI velocities. They have tried to correct them by forward and reverse integration in time. In fact one of the major limitations of our initial effort [19] is that regions of interest have to be very carefully chosen. It is crucial that the trajectory of the region of interest never include velocities from the flowing blood in the ventricle, or velocities from outside the heart. However, since errors in the region positions usually grow in time, the path of the region of interest often leaves the endorcadial wall and enters the ventricle, or goes outside of the myocardium. It is clear, that information about the myocardium boundaries needs to be added. Another related problem in [19] is the inability to couple the regions of interest during the tracking: regions close to each other at the initial instant will eventually overlap, and collide during the tracking process. These problems provided the motivation to propose a more ambitious scheme that could track the complete geometry of the LV. In fact very little work has been expended on the subject of nonrigid motion recovery of a complete object from a sequence of velocity fields. It is a difficult problem because it is nonlinear and unstable. However it is an important problem since there are many different ways to acquire velocity information: phase contrast MRI, Doppler ultrasound, optical flow, and others.

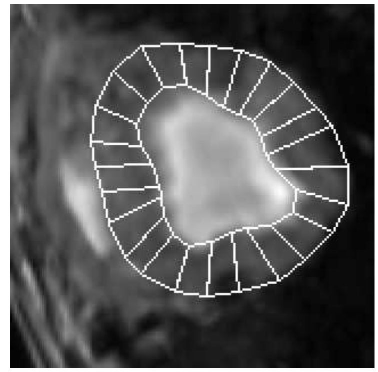

Fig. 1. Decomposition of the myocardium into elementary cells. The nodes $\{\xi_i\}$ are material points at the intersection of the cells. The decomposition is initialized at time 0, and is deformed at successive instants. The displacements of the nodes completely characterize the motion of the myocardium.

The major contribution of this work is to explore and propose a completely new framework to track the entire LV from a sequence of velocity fields, and a sequence of contours. Our approach relies on the statistical techniques of estimation theory ; these provide indeed the backbone of tracking and data association techniques [23], and have been used quite successfully in a related problem in the same area [24].

The paper is organized as follows. In the next section we describe the method. Results of experiments conducted on simulated data, phantom data, and *in vivo* data are given in Section III. A discussion about the method is given in Section IV.

II. Methods

A. Overview of the algorithm

The tracking algorithm utilizes two temporal sequences of data: (i) a time sequence of 16 velocity fields (the heart cycle is divided into 16 instants) ; and (ii) a time sequence of 16 contours of the LV: the endocardium (inner contour) and the epicardium (outer contour). In this paper the time sequence of velocity fields is obtained using a gated phase contrast cine-gradient echo acquisition. The contours of the LV are extracted from the sequence of the 16 magnitude images of the same MR sequence.

The geometry of the myocardium is characterized by a deforming mesh composed of N nodes $\xi_1, \dots, \xi_N$. The partition is composed of quadrilaterals (see Fig. 1). Each quadrilateral has two nodes on the endocardium and two nodes on the epicardium. We assume that the kinematic state of the LV can be accurately characterized, at any instant, by a spatial piecewise polynomial approximation of the phase-contrast velocity field. This "spline-vector" approximation is uniquely characterized by a basis of N functions $\{\Phi_i\}_{i=1,\dots,N}$ (one for each node) with local support (see Fig. 2).

We assume that the support of each basis function is

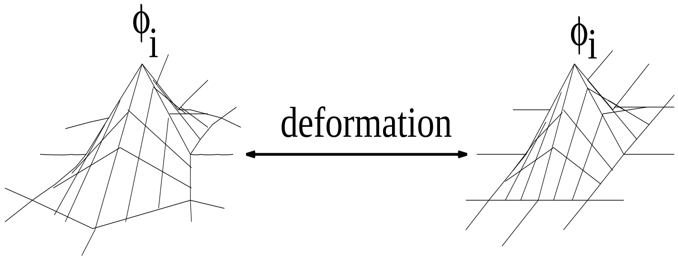

Fig. 2. At each instant we approximate the spatial velocity over a space of basis functions Φ_i which are moving along with the deformation of the domain Ω.

moving along with the deformation of the domain (see Fig. 2). We have

$$\Phi_i(\mathbf{x}(\xi_i, k)) = 1 \qquad \forall k = 0, \ldots, T \tag{1}$$

where $\mathbf{x}(\xi_i, k)$ is the two-dimensional position of the node ξ_i at time k.

Let $\mathbf{W}$ be the space spanned by the basis functions $\{\Phi_i\}$. Let $\mathbf{v} = (u, v)$ be the spatial velocity field at time k ; this velocity field is the k-th velocity field generated by the MR acquisition sequence. We define $(u^\star, v^\star)$ as the spline-vector approximation of (u, v) over $\mathbf{W} \times \mathbf{W}$. $(u^\star, v^\star)$ can be expanded into the basis $\{\Phi_i\}$

$$u^\star(x) = \sum_{i=1}^{N} u_i^\star \Phi_i(x) \qquad v^\star(x) = \sum_{i=1}^{N} v_i^\star \Phi_i(x) \tag{2}$$

where $(u_i^\star, v_i^\star)$ is the nodal value of the velocity for the node ξ_i.

For each node ξ_i we define a state vector, $\mathbf{s}_i$, that characterizes the "true" value of the node's kinematics. We will not be able to calculate directly $\mathbf{s}_i$, but we will derive *measurements* related to $\mathbf{s}_i$ at every instant k. For each node, we construct a measurement vector, $\mathbf{m}_i$, composed of two components: position, and velocity. The velocity component is the nodal value of the velocity $(u_i^\star, v_i^\star)$. The position component is derived from the contours of the LV at time k. The measurements are corrupted observations that are related to the "true" kinematics of the node.

Our goal is to process the measurements $\{\mathbf{m}_i(0), \ldots \mathbf{m}_i(k), i = 1, .., N\}$ in order to obtain the best estimate of $\{\mathbf{s}_i(k), \quad i = 1, .., N\}$, the kinematic state of the LV at time k. Assuming that the motion of the myocardium is governed by a set of differential equations, we can derive a model of the LV's dynamic behavior. The mathematical tools that provide a solution to the problem of estimating the state of the LV, given the measurements, are the statistical techniques of estimation theory [23], [25]. We use a temporal smoothing filter that generates smooth estimates of $\mathbf{s}_i$, for each node ξ_i of the mesh. We note that intuitively the goal of position measurements is to "anchor" the tracking, and prevent it from drifting due to errors in numerical integration of the velocity. Formulating this problem as an estimation problem makes it possible to integrate position information and velocity information into a consistent framework. As a result, the method will be much more reliable, and more accurate than our previous effort [19].

B. Data acquisition

Velocity maps. Sixteen velocity maps and magnitude images are acquired over the heart cycle, using a technique, termed *phase contrast cine magnetic resonance imaging* (PC MRI) [1], [26]. The technique combines phase contrast imaging methods [18] with cardiac cine techniques. Phase contrast imaging can deliver quantitative measurement of motion. The technique exploits the fact that when a magnetic field gradient is applied, the phase change of moving spins is different from the phase change of stationary spins. Although conventional MRI only exploits the magnitude of the NMR (Nuclear Magnetic Resonance) signal, the phase can carry motion information. As explained in [1], [19], spins moving with a velocity ν experience a phase shift φ proportional to the velocity ν and proportional to the first moment of the gradient waveform $G(t)$ (measured during TE, the echo delay time):

$$\varphi = \nu\gamma \int_0^{TE} t\, G(t) dt \tag{3}$$

Where γ is the gyromagnetic ratio. The velocity can then be estimated in a particular direction by measuring difference in phase shift between two acquisitions made with a different first moment. The velocity in three orthogonal directions can be measured for each voxel in the image. Exploitation of the phase shift φ in (3) is the basis of phase contrast MRI. However, the effects of eddy currents may alter the gradient waveform $G(t)$, and therefore, influence phase changes. As a result, velocity measurements will be corrupted by an additive error. A non zero velocity will be measured in regions known to be static. The error is usually a slowly varying function of the spatial and temporal coordinates. It can be approximated by a linear function across the image. A least-squares fit to the velocity is performed in regions known to be static. The resulting linear model is subtracted at each point in the image [1], [27], [19].

We emphasize the case where velocity measurements are obtained by PC MRI, although we note that velocities can be directly estimated from the spatiotemporal changes of the intensity function [9], [16], [17].

Contours extraction. At any given instant we have access to the magnitude image of the PC MRI sequence, and we extract the contours of the myocardium using the deformable contour/region growing approach presented in [28].

C. Measurement definition

We explain here, how we calculate a measurement of the nodes' kinematics, from the data described above, at every time sample. The velocity field $\mathbf{v} = (u, v)$ that we obtain at time k from the PC MRI sequence is composed of Eulerian velocities: they provide a spatial description of the velocity field at each instant. $\mathbf{v}(\mathbf{x}, k)$ is the velocity of a material point that occupies the position $\mathbf{x}$, at time k ; however, we can not identify this material point. In order to build a kinematic measurement for each node ξ_i at time k, we

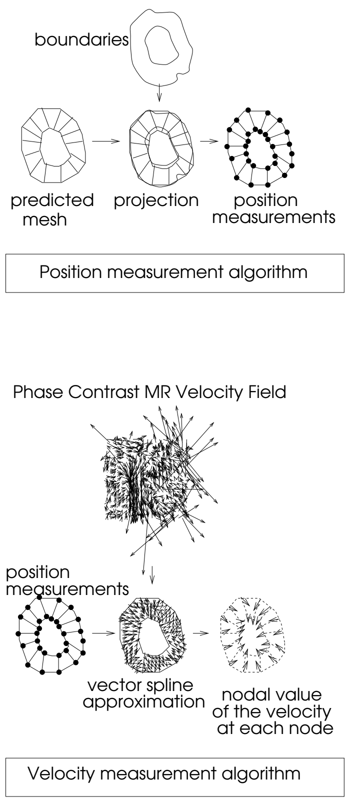

Fig. 3. Top: position measurement, Bottom: velocity measurement. The position measurement is used as an input for the velocity measurement algorithm.

need to calculate the Lagrangian velocity, $\mathbf{v}_i$, of the node:

$$\mathbf{v}_i(k) = \mathbf{v}(\mathbf{x}(\xi_i, k), k) \tag{4}$$

where $\mathbf{x}(\xi_i, k)$ is the two-dimensional position of the node at time k.

To achieve this, we first match the LV geometry (defined by the contours of the LV) at the current instant with a prediction of the mesh geometry, generated by the tracking algorithm (see Fig 3).

Each node of the predicted mesh is projected onto the extracted contours (see Fig 3). This defines the position measurement for this node, at the current instant. Ideally this measurement should correspond to an estimate of the position of the material point ξ_i. There can be an uncertainty (due to the inexact map between the nodes of the mesh and the contours) in addition to the inaccuracy on the contours. We now have a measurement $(\tilde{x}_i, \tilde{y}_i)$ of the two-dimensional position $\mathbf{x}(\xi_i, k)$ of each node ξ_i at time k.

C.1 Vector spline approximation of the velocity field

Using the mesh defined by the projected nodes, we then calculate the nodal value of the velocity $(u_i^\star, v_i^\star)$ at each node (see Fig 3) using a vector spline approximation method. Inside each quadrilateral of the mesh, a bilinear model of the velocity describes the transmural variation of the velocity across the wall.

Figure 4 shows a cross section of the velocity across the myocardium at time $t = 9$. The limited transmural resolution of the data (on the average we only have access to 6 to 8 pixels across the wall) makes it difficult to fit higher order models. The vector spline approximation technique is an extension of the one-dimensional spline least squares approximation method [29]. We refer to [29] for details on this classic method. We note that a smoothing functional that incorporates the *divergence-free constraint* and the *incompressibility constraint* [17] could be easily included in our approximation framework. However the validity of the *incompressibility constraint* for the left ventricle (LV) remains questionable [30] in the the 3-D case, and is not valid in 2-D. Therefore we do not choose to use it at this time.

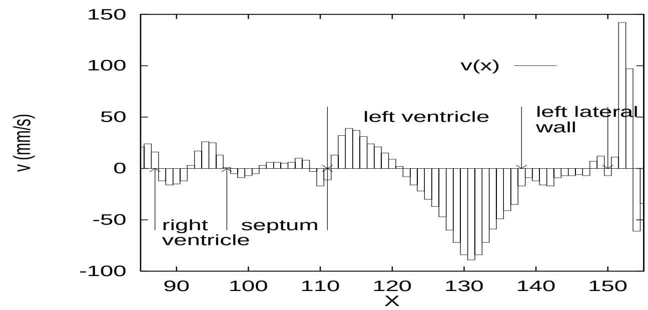

Fig. 4. Cross section of the y component of the velocity field at time $= 9$. $v(x, y)$ is plotted against x for the same $y = 128$. This corresponds to an horizontal line in the middle of the myocardium in figure 8.

C.2 The measurement vector

At this point we can construct a measurement vector $\mathbf{m}_i$ for each node ξ_i. We give here the equations of $\mathbf{m}_i$ for one component, x for instance. Similar relations can be derived for y. We have

$$\mathbf{m}_i = \begin{bmatrix} \tilde{x}_i \\ u_i^\star \end{bmatrix} \tag{5}$$

where $(u_i^\star, v_i^\star)$ is the nodal value of the velocity, and $\tilde{x}_i$ is position measurement.

D. Model of the dynamic behavior of the mesh

We describe here the model of the LV's dynamic behavior. We use this model to characterize the temporal evolution of the mesh. In this work, as in most other cardiac applications, we assume the motion of the heart is periodic. We can expand the trajectory of each node ξ_i into a basis of sine functions. Exploiting a Fourier expansion of the trajectory has been proposed in our recent work [31], and also in [32]. Due to the problem of limited temporal resolution (16 time samples only are available at the moment), high order terms tend to be difficult to estimate. We only retain the first two terms of the expansion. For the clarity of the presentation and to lighten the notation, from now on we drop the index i of the node ξ_i wherever it can be done without causing confusion. A continuous model of the the trajectory of the node ξ,

$$\mathbf{x}(t) = \mathbf{x}(\xi, t) \tag{6}$$

is thus given by

$$\mathbf{x}(t) = \bar{\mathbf{x}} + A \sin(2\pi\omega t + \varphi) \qquad t \in \mathbb{R} \tag{7}$$

where t is the continuous time index, $\bar{\mathbf{x}}$ is the mean position over the period, and A is the amplitude of the motion. The frequency of the oscillator is $2\pi\omega = 2\pi/T$ where T is the period of the heart cycle. The geometric interpretation of (7) is that the trajectory of the node is approximated by an ellipse. This system model is only valid over a short time interval. Similarly, models that assume that the velocity [19], [21], or the acceleration [22] are constant between two instants, are inappropriate for longer durations. As opposed to the constant-velocity, or constant-acceleration models, (7) explicitly models the trajectory as being closed. Furthermore, we can introduce a "fading memory" factor in the tracking filter so that the estimate of $\mathbf{s}$ is based only on the most recent measurements. Finally, we also add some noise in the model (7) to accommodate significant differences between (7) and the real motion of the myocardium.

From (7) we derive the following linear dynamic system that describes the discrete time evolution of $\mathbf{x}(t)$ We give the equations for one component of $\mathbf{x}$, x for instance. Let $\mathbf{s}(k) = [\bar{x}, x, \dot{x}]^T(k)$ be the state vector that describes the x component of the node ξ at time k. We have

$$\mathbf{s}(k+1) = \mathbf{F}\,\mathbf{s}(k) + \boldsymbol{\zeta}(k) \tag{8}$$

with

$$\mathbf{F} = \begin{bmatrix} 1 & 0 & 0 \\ 1-\cos(\omega\Delta t) & \cos(\omega\Delta t) & \frac{1}{\omega}\sin(\omega\Delta t) \\ \omega\sin(\omega\Delta t) & -\omega\sin(\omega\Delta t) & \cos(\omega\Delta t) \end{bmatrix} \tag{9}$$

where $\boldsymbol{\zeta}(k) = [\zeta_1, \zeta_2, \zeta_3]^T(k)$ is a zero mean Gaussian noise of covariance matrix $\mathbf{Q}(k)$; and where Δt is the time interval between two time samples. The assumption of Gaussian noise is not completely realistic– it is an approximation. Let $\mathbf{\Pi}(k)$ be the covariance matrix of $\mathbf{s}(k)$. From (8)we have

$$\mathbf{\Pi}(k+1) = \mathbf{F}\mathbf{\Pi}(k)\mathbf{F}^T + \mathbf{Q}(k) \tag{10}$$

where $\mathbf{F}^T$ is the transpose of $\mathbf{F}$. The initial value of $\mathbf{\Pi}$,$\mathbf{\Pi}(0) = \mathbf{\Pi}_0$ is supposed to be known. With our definition of the state vector, and from (5) the measurement system takes the form

$$\mathbf{m}(k) = \mathbf{H}\mathbf{s}(k) + \boldsymbol{\eta}(k) \quad \text{with} \quad \mathbf{H} = \begin{bmatrix} 0 & 1 & 0 \\ 0 & 0 & 1 \end{bmatrix} \tag{11}$$

where $\boldsymbol{\eta} = [\eta_1, \eta_2]^T(k)$ is a zero mean Gaussian noise vector of covariance matrix $\mathbf{R}(k)$. Equation (11) tells us that we can only measure the position and the velocity of each node ; the mean position ($\bar{\mathbf{x}}$) can not be measured.

The problem is then the following: Given the observations : $\mathbf{m}(0), \ldots, \mathbf{m}(T)$, we wish to obtain an optimal estimate of the state vector $\mathbf{s}$ at any given time k within the interval, $\mathbf{s}(k|k)$, that minimizes the mean-norm-squared-error. There exists an efficient recursive algorithm to calculate this estimate: the fixed interval smoothing filter [25], [33], [34]. In the next section we provide a brief description of a particular implementation of the algorithm that relies on two filters.

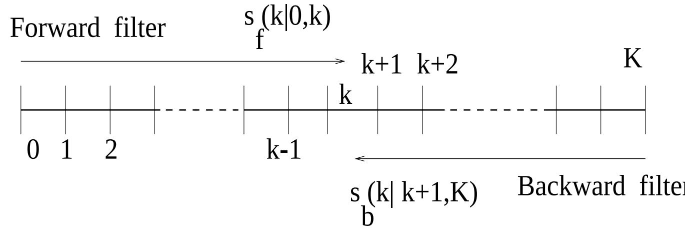

Fig. 5. Flow chart of the forward and backward filters operation. The forward filter generates the optimal estimate at time k, $\hat{\mathbf{s}}_f(k|0,k)$, based upon all the measurements from time 0 to time k. The backward filter generates $\hat{\mathbf{s}}_b(k|k+1,T)$, the optimal estimate at time k based upon all the measurements from time $k{+}1$ to time T. The smoothed estimate, $\hat{\mathbf{s}}_s(k)$, based upon all the measurements from time 0 to time T, is generated by optimally combining the value of the forward filter and the value of the backward filter at time k.

E. Optimal temporal smoothing of the nodes trajectory

The optimal linear smoother is a combination of two optimum linear filters. One which works forward over the data, and the other which runs backward. The forward filter processes the data from time 0 to some time k within the interval, and generates the optimal estimate $\hat{\mathbf{s}}_f(k|0,k)$ as well as $\mathbf{P}_f(k|0,k)$, the covariance matrix of $\hat{\mathbf{s}}_f(k|0,k)$. Similarly, the backward filter generates $\hat{\mathbf{s}}_b(k|k+1,T)$, the optimal estimate at time k based upon all the measurements from time $k+1$ to time T as well as $\mathbf{P}_b(k|k+1,T)$, the covariance matrix of $\hat{\mathbf{s}}_b(k|k+1,T)$.

Together these two filters utilize all the available information. The smoothed estimate $\hat{\mathbf{s}}_s(k)$, based upon all the measurements from time 0 to time T, is generated by optimally combining the value of the forward filter and the value of the backward filter at time k [25], [33], [34] (see Fig. 5). We have

$$\hat{\mathbf{s}}_s(k) = \mathbf{P}_s^{-1}(k)\left[\mathbf{P}_f^{-1}(k|0,k)\hat{\mathbf{s}}_f(k|0,k) \quad + \right. \\ \left. \mathbf{P}_b^{-1}(k|k+1,T)\hat{\mathbf{s}}_b(k|k+1,T)\right] \tag{12}$$

where $\mathbf{P}_s(k)$, the covariance matrix of $\hat{\mathbf{s}}_s(k)$, is given by

$$\mathbf{P}_s^{-1}(k) = \mathbf{P}_f^{-1}(k|0,k) + \mathbf{P}_b^{-1}(k|k+1,T) \tag{13}$$

Equation (12) indicates that the forward and backward estimates are weighted according to the confidence we have in the precision of each, and combined to generate the smoothed estimate. Equation (13) shows that

$$\mathbf{P}_s(k) \leq \mathbf{P}_f(k|0,k) \tag{14}$$

which indicates that the smoothed estimate is at least as good as the filtered estimate. In fact as shown previously within a simpler deterministic framework [19], [21], forward/backward integration usually performs better than forward integration only.

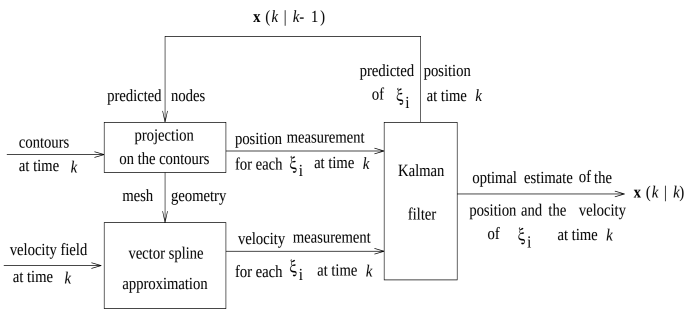

Fig. 6. Flow chart of the forward (or backward) filter algorithm at time k. The ξ_i $i = 1, \ldots, N$ are the nodes of the partition. The incoming data: contours and velocity fields are shown on the left. The position measurement is calculated using the predicted position of the node ξ_i at time k: $\mathbf{x}(k|k-1)$, as explained in Fig. 3. This prediction is generated by the Kalman filter. The vector spline approximation of the PC MRI velocity filed yields a nodal value of the velocity at each node ξ_i, as explained in Fig. 3. Finally the Kalman filter updates the predicted position, and velocity with the measurement at time k. It generates the optimal estimate $\mathbf{x}(k|k)$.

E.1 Optimal forward filtering: the Kalman filter

The optimal forward estimate $\hat{\mathbf{s}}_f(k+1|0,k+1)$ is generated by filtering data prior to time k with a Kalman filter [25].

Figure 6 represents the calculations schematically. We have

$$\hat{\mathbf{s}}_f(k+1|0,k+1) = \hat{\mathbf{s}}_f(k+1|0,k) + \mathbf{K}(k+1)\left[\mathbf{m}(k+1) - \mathbf{H}\hat{\mathbf{s}}_f(k+1|0,k)\right] \quad (15)$$

where $\hat{\mathbf{s}}_f(k+1|0,k)$, the prediction of the state vector at time $k+1$ is given by

$$\hat{\mathbf{s}}_f(k+1|0,k) = \mathbf{F}\mathbf{s}_f(k|0,k) \quad (16)$$

Equation (15) consists in updating the prediction with the new measurement $\mathbf{m}(k+1)$. The gain matrix $\mathbf{K}(k+1)$ controls the relative importance of the measurement with respect to the prediction. We have

$$\mathbf{K}(k+1) = \mathbf{P}_f^T(k+1|0,k)\left[\mathbf{P}_f^T(k+1|0,k) + \mathbf{R}(k+1)\right]^{-1} \quad (17)$$

where $\mathbf{P}_f(k+1|0,k)$ is the covariance matrix of the prediction $\hat{\mathbf{s}}_f(k+1|0,k)$. Also, we have

$$\mathbf{P}_f(k+1|0,k) = \mathbf{F}\mathbf{P}_f(k|0,k)\mathbf{F}^T + \mathbf{Q}(k) \quad (18)$$

and

$$\mathbf{P}_f(k+1|0,k+1) = \left[\mathbf{I} - \mathbf{K}(k+1)\right]\mathbf{P}_f(k+1|0,k) \quad (19)$$

where $\mathbf{I}$ is the 2×2 identity matrix. We note in (17) that if $\mathbf{R}(k+1)$, the covariance of the measurement, has very large components with respect to $\mathbf{P}_f(k+1|0,k)$, the covariance of the prediction, then $\mathbf{K}(k+1)$ is very small. Then $\hat{\mathbf{s}}_f(k+1|0,k+1)$ given by (15) essentially ignores the new measurement $\mathbf{m}(k+1)$, and is almost equal to the prediction. If $\mathbf{R}(k+1)$ has very small components with respect to $\mathbf{P}_f(k+1|0,k)$, then $\mathbf{K}(k+1)$ is almost equal to $\mathbf{I}$, and $\hat{\mathbf{s}}_f(k+1|0,k+1)$ is almost equal to $\mathbf{m}(k+1)$. The gain matrix is "proportional" to the uncertainty in the prediction, and "inversely proportional" to the measurement noise.

Choice of $\mathbf{R}(k)$ and $\mathbf{Q}(k)$

We model $\mathbf{R}(k)$ as a diagonal matrix. The first term on the diagonal is the variance of the position measurement, and it is proportional to the inverse of the magnitude of the gradient of the magnitude signal. A large value of the gradient indicates a large confidence in the local contour. The second term on the diagonal of $\mathbf{R}(k)$ is the variance of the velocity, and it can be calculated using the method presented in [35]. Phase difference reconstruction has been used during the experiments. The variance of $\mathbf{v}$ is given by

$$\sigma_{\mathbf{v}} = \frac{\sigma}{M} \quad (20)$$

where M is the magnitude signal, and σ is the variance of this signal. However when using this approach, large random vectors on the epicardium, and large flow vectors in the ventricle had very small variance. To combat this problem we have used a fixed uniform variance for any velocity measurement inside the myocardium.

We model $\mathbf{Q}(k)$ as a diagonal matrix. The values of $\mathbf{Q}(k)$ can be adjusted to obtain different levels of temporal smoothing. For all experiments we took the same value of $\mathbf{Q}(k)$. We have chosen a large $\mathbf{Q}(k)$ in order to follow closely the measurements.

There is a bootstrapping mode to initialize the filter. At the first instant (time 0) we use the position and velocity measurements to initialize the last two components of $\mathbf{s}(0)$. However it requires a second time step (time 1) to get an estimate of the acceleration (using the velocity difference). Since the mean position ($\bar{\mathbf{x}}$) is proportional to the acceleration, we thus obtain an estimate of the first component of $\mathbf{s}(0)$. During the bootstrapping mode, the estimates may be quite noisy, as shown in the experiments.

E.2 Optimal backward filtering: a backward Markovian model

The discrete-time system (8) propagates forward in time. In order to build the backward estimate, it would be useful to consider time running backward. However a backward representation of (8) cannot be obtained simply by just reversing the direction of time in a forward Markovian representation as (8) [33], [34]. Nevertheless it is possible to build a process equivalent to (8) up to second order properties, but with the state model propagating in reverse time [33], [34]. The reverse time model corresponding to (8) is given by [33], [34]:

$$\mathbf{s}_b(k) = \mathbf{F}_b(k+1)\mathbf{s}_b(k+1) + \boldsymbol{\zeta}_b(k+1) \quad (21)$$

where $\boldsymbol{\zeta}_b(k)$ is a zero mean Gaussian noise of covariance matrix $\mathbf{Q}_b(k)$. We have the following expression for $\mathbf{Q}_b(k)$ and $\mathbf{F}_b(k+1)$

$$\mathbf{F}_b(k+1) = \mathbf{F}^{-1}(k)\left[I - \mathbf{Q}(k)\mathbf{\Pi}^{-1}(k+1)\right] \quad (22)$$

$$\mathbf{Q}_b(k+1) = \mathbf{F}_b(k+1)\mathbf{Q}(k)\mathbf{F}_b^T(k+1) \quad (23)$$

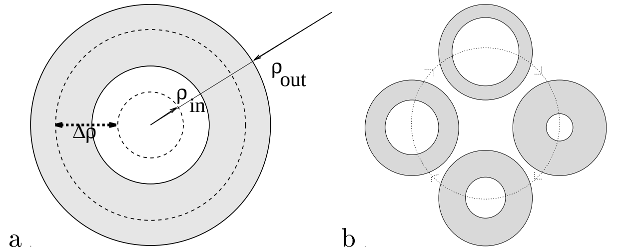

Fig. 7. Models of myocardium used in validating the tracking algorithm. Left: (a) A 2-D annulus undergoes periodic motion. The outer edge remains stationary while the internal radius $\rho(k)$ is evolving periodically. The velocity varies linearly from the outer edge to the inner edge. Right: (b) In this simulation the periodic change in the inner edge is the same as in the model on the left. However, the complete annulus is now translating in the plane with a periodic motion. The trajectory of the center of the annulus is a circle.

where $\mathbf{\Pi}(k)$ is the covariance matrix of $\mathbf{s}$ at time k, defined in (10). Kalman filtering can then be used on the system (21) to generate the optimal estimate of $\mathbf{s}(k)$ given measurements from time $k+1$ to time T.

III. Experiments

A. Numerical simulations

A quantitative evaluation of the method has been performed using numerical simulations of velocities and contour data. The simulated velocity fields are representative of the motion of the myocardium in a general way. The simulation is not designed to model the complex motion of the LV, but to provide a controlled method for quantitative evaluation of the approach under a wide range of conditions. For both experiments the velocity components were coded as integers. Therefore truncation errors resulted in noise on the velocity fields.

A.1 Periodically contracting annulus simulation

Here a 2-D annulus undergoes periodic motion (see Fig. 7a). The outer edge remains stationary while the internal radius $\rho(k)$ is evolving according to

$$\rho(k) = \rho(0) + \lambda(\rho(0)) \sin(\omega t) \Delta\rho \tag{24}$$

with

$$\lambda(\rho(0)) = \frac{\rho_{out} - \rho(0)}{\rho_{out} - \rho_{in}} \tag{25}$$

with $\omega = 2\pi\frac{100}{60}$, $\rho_{out} = 40\ pixels$, $\rho_{in} = 14\ pixels$, $\Delta_\rho = 2.5\ pixels$, with an effective heart rate of 100 $beats/min$. 16 images were simulated, representing one heart cycle. The velocity varies linearly from the outer edge to the inner edge. The motion of the annulus was tracked using 16 nodes on the inner contour and 16 nodes on the outer contour. The position of the tracked nodes have been compared to the theoretical values (determined analytically). Two different errors were calculated: a root mean squared (RMS) error over all nodes, at each instant ; and a relative error over the total path length, for each node. The RMS error was calculated at each instant k. The average was then taken over all nodes

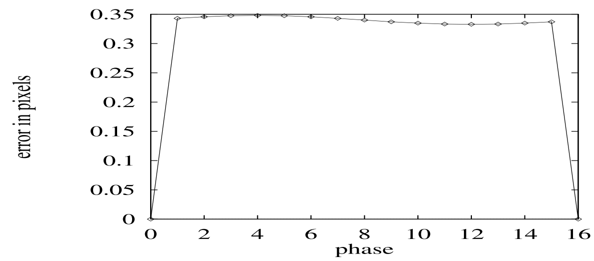

Fig. 8. Expanding annulus: RMS tracking error at each instant k. The average was taken over all nodes.

$$\text{RMS error}(k) = \sqrt{\frac{1}{N}\sum_{i=1}^{N} \|\mathbf{x}_i(k) - \hat{\mathbf{x}}_i(k)\|^2} \tag{26}$$

where $\mathbf{x}_i(k)$ is the true position of the node ξ_i, and $\hat{\mathbf{x}}_i(k)$ is the result of the tracking. The relative error was calculated for each node i. The average was taken over the heart cycle

$$\text{relative error}(i) = \frac{\sqrt{\frac{1}{T}\sum_{k=0}^{T} \|\mathbf{x}_i(k) - \hat{\mathbf{x}}_i(k)\|^2}}{\int_0^T d\mathbf{x}_i} \tag{27}$$

where $\int_0^T d\mathbf{x}_i$ is the total path length of the node i. The mean relative error over all the nodes was then calculated.

Fig. 8 shows the RMS error (in pixels) over the heart cycle. The estimate build at the second time step (time 1) is calculated using the bootstrapping mode, and thus relies only on the velocity measured at time 0. The quantization error on the velocity results in a noisy velocity measurement at time 0. Consequently, the position estimate at time 1 does not coincide with the true position, as shown on trajectories pointed by arrows in Fig. 9.

We note in Figure 9 that after two time steps (necessary for the Kalman filter to switch from the bootstrapping mode to the steady state mode) the temporal smoothing performed by the filter allows us to estimate a trajectory that is visually correct. However, due to the error in the position at time 1, the rest of the path is globally translated from the theoretical trajectory (defined as a path perpendicular to the initial position at time 0). This systematic error creates a small RMS error. The mean relative error over all the nodes was 0.9% of the total path length. Given the amplitude of the motion there is a good agreement between the results of the tracking and the theoretical values.

A.2 Periodically expanding and translating annulus simulation

In this simulation the periodic change in the inner edge is the same as in the model above. However, the complete annulus is now translating in the plane with a periodic motion (see Fig. 7b). The trajectory of the center of the annulus is a circle:

$$\begin{aligned} x_c &= x_0 + \Delta_c \cos(\omega t) \\ y_c &= y_0 + \Delta_c \sin(\omega t) \end{aligned} \tag{28}$$

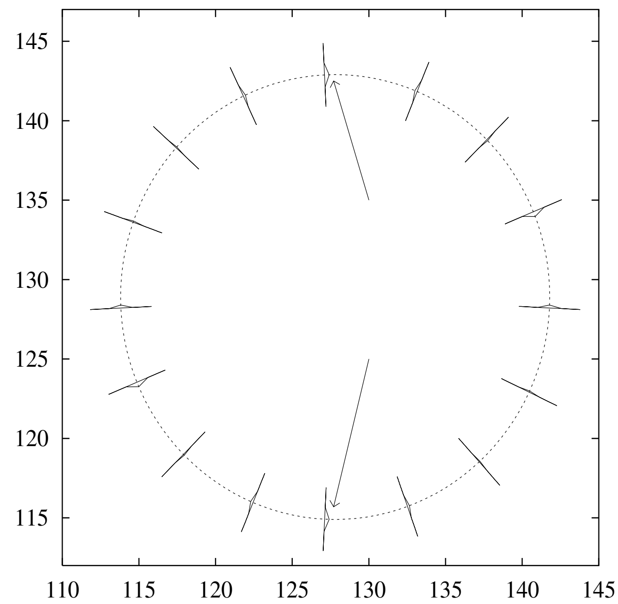

Fig. 9. Expanding annulus: trajectories of all nodes located on the inner contour. The inner contour at time 0 has been drawn. For two specific nodes, arrows point towards the initial position of the nodes. The position estimate at time 1 does not coincide with the "true" position. Consequently, the rest of the path is globally translated from the theoretical trajectory (defined as a path perpendicular to the initial position at time 0). After two time steps the temporal smoothing yields a trajectory that is visually correct.

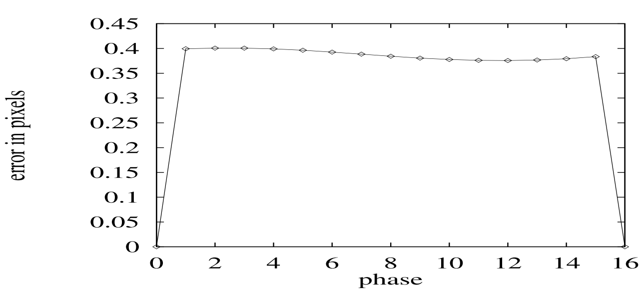

Fig. 10. Expanding and translating annulus: RMS tracking error at each instant k. The average was taken over all nodes.

with $\Delta_c = 2.5 pixels$. As in the previous model the velocity varies linearly from the outer edge to the inner edge. The motion of the annulus was tracked using 16 nodes on the inner contour and 16 nodes on the outer contour. Errors in the position of the tracked nodes have been evaluated.

Figure 10 shows the RMS error, in pixels, for any phase over the cycle. As in the previous example, the position estimate at the second time step (time 1) does not coincide with the expected position at this instant. Consequently, the path is globally translated from the theoretical trajectory (defined as a path perpendicular to the initial position at time 0). Again, this systematic error in the position estimates creates a small RMS error. The mean relative error over all the nodes was 1.8% of the total path length. Given the magnitude of the motion, the agreement between the measured data and the theoretical values is good.

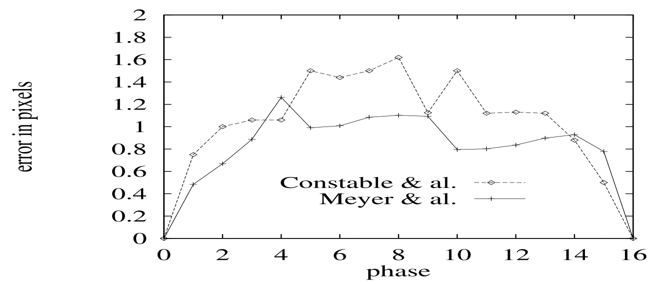

Fig. 11. Phantom data: RMS tracking error at each instant k, in the solid line. The average RMS error in tracking four small regions of interest using the method proposed in Constable et Al. [19] is also shown in the dashed line.

B. Phantom study

In order to judge quantitatively the accuracy of the algorithm with PC MRI data, we have performed an experiment with a phantom. The phantom consisted of a gel-filled disk undergoing rotation and translation in the plane. The maximum translation was $1cm$, and the maximum rotation was 20^o. The motion of the phantom was periodic with an effective heart rate of $66 beats/min$. The phantom was imaged in a quadrature head coil using a cine PC gradient echo imaging sequence with the maximum velocity encoding in all three spatial directions set to $150 mm/s$. The imaging parameters were: flip angle $= 30^o$, TE (echo time) $= 11ms$, TR (pulse repetition time) $= 22ms$, FOV (field of vue) $= 30cm$, $8mm$ slice thickness, a 256×128 matrix, and 4 nex. The background velocity offset induced by eddy currents was estimated and subtracted in each frame before tracking the motion. The disk had four small markers on its outer edge. The trajectories of the markers have been manually hand traced, and using triangulation, the theoretical position of any point inside the phantom could be calculated at any instant. The standard deviation for the theoretical position of the nodes was 1 pixel. We put 16 nodes on the inner contour and 16 nodes on the outer contour. RMS errors in the position of the nodes using the proposed approach have been calculated at each instant, and are shown in Fig. 11. The average RMS error in tracking four small regions of interest using the method proposed in [19] is also shown in Fig. 11. This experiment demonstrates that our new approach can track a complete object with more accuracy than the method proposed in [19]. However the method proposed in [19] is quite different from our new method. In [19] the error corresponds to four selected regions of 3×3 pixels. Regions located at a particular position may show a small error, while others may show larger error, due for instance to a larger motion magnitude. In our case the error really takes into account every point in the tracked object. Furthermore, the phantom experiment is an easy experiment for both methods. The real benchmark for both methods is the *in-vivo* study, where the method presented in [19] often fails to yield a proper path for the region– since the region leaves the myocardium.

The mean relative error over all the nodes was 4.4% of

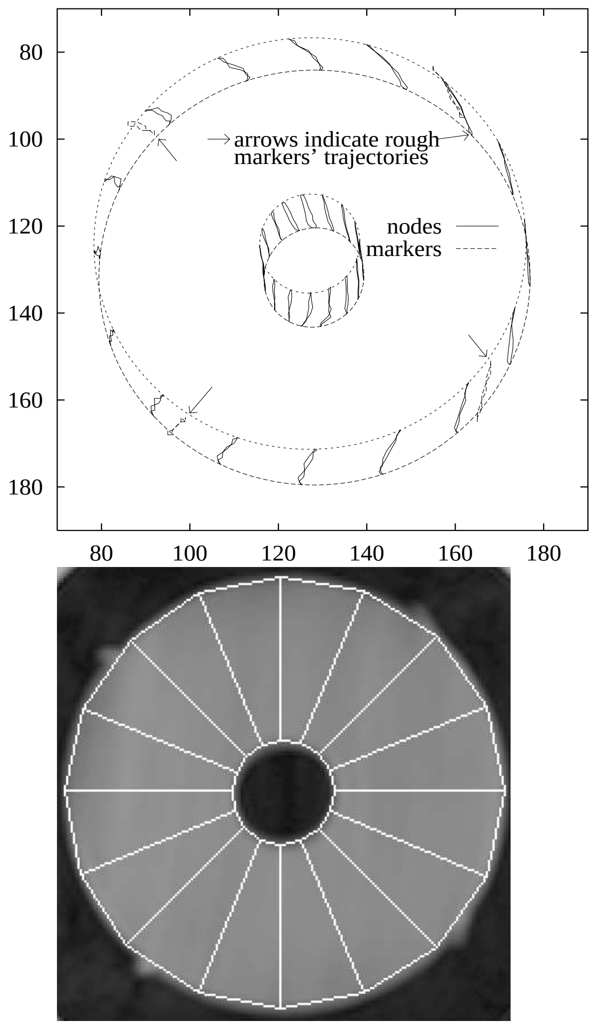

Fig. 12. Top: trajectories of the tracked nodes and trajectories of the hand-traced markers. The contours of the phantom are superimposed at time 4 and at time 12 only, and the axes are labelled in pixel units. Bottom: phantom at instant 0, with superimposed partition.

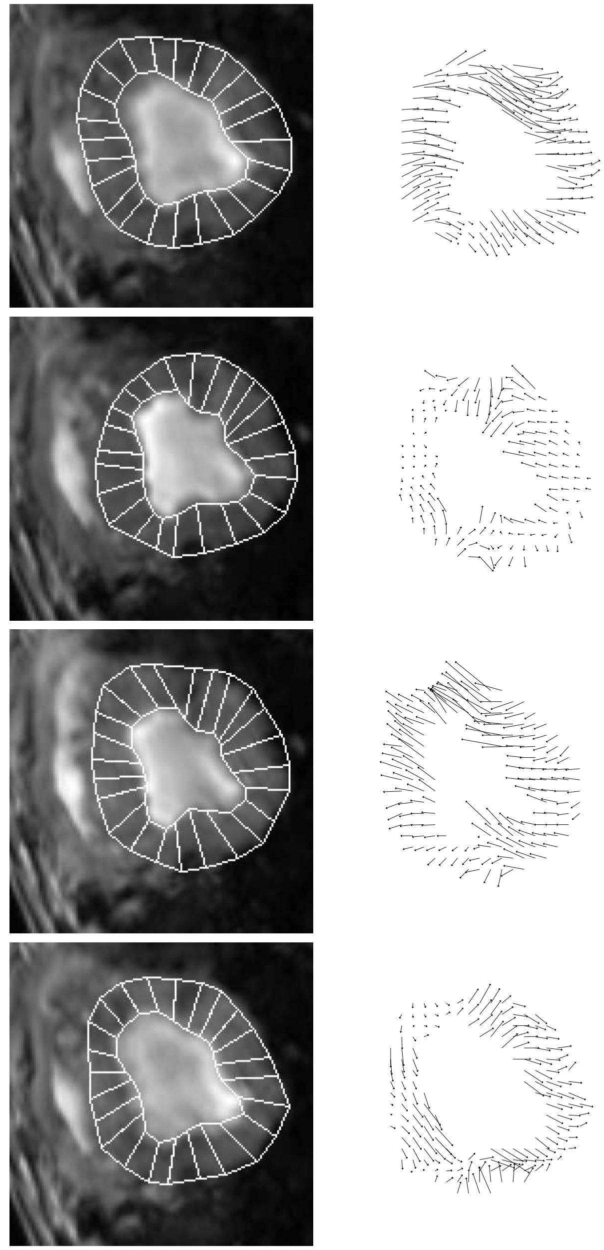

Fig. 13. *in vivo* canine study, pre-infarct. Left: results of the tracking at time 1, 5, 9, and 14. Right: vector spline approximation of the velocity field at time 1, 5, 9, and 14. The tracking started at time 0 (end diastole)

the total path length. Given the initial error on the theoretical positions of the nodes, the calculated positions are in good agreement with the true values. The trajectories of the nodes, and the trajectories of the markers are shown in Fig. 12. The contours of the phantom at time 4 and at time 12 are also shown.

C. In Vivo Data

To further validate our approach, the tracking algorithm has been tested *in vivo* with an open chest canine model of infarction. This experiment was part of an ongoing study aimed at examining the effects of infarct on myocardial motion parameters [4], [19]. A dog was positioned in a quadrature head coil for MR imaging. Three contiguous short axis slices were collected using the cine PC gradient echo sequence. Velocity maps were acquired both before and one hour after a permanent occlusion of the proximal left anterior descending artery (LAD). The imaging parameters were flip angle = 30^o, $TE = 11ms$, $TR = 34ms$, $FOV = 28cm$, $5mm$ skip 0, a 256×128 matrix and 4 nex, venc = $15cm/s$. Average heart rate was $120bpm$ before the coronary occlusion and $132bpm$ after occlusion. We recognize that the motion of the myocardium is three-dimensional. We consider here a simplified 2-D version of the problem.

The LV has been tracked before the coronary occlusion with a partition consisting of 24 nodes on the endocardium and 24 nodes on the epicardium. The tracking started at time 0 (end diastole) when the wall was the thinnest. The nodes were initially equally sampled along each contour.

Figure 13 (left) shows the deformed partition at four instants through the cardiac cycle. The fitted spline vector

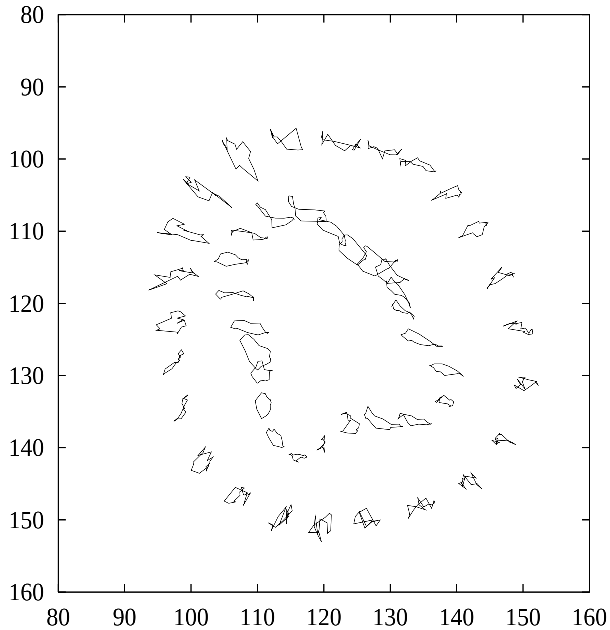

Fig. 14. *In vivo* canine study, pre-infarct, trajectories of the nodes.

field is shown in Fig. 13 (right) at the corresponding instants. The trajectories of the nodes are shown in Fig. 14.

After occlusion of the LAD the LV has been tracked with a similar partition and the same number of nodes.

Figure 15 (left) shows the deformed partition at four instants through the cardiac cycle. The fitted spline vector field is shown in Fig. 15 (right) at the corresponding instants. We note the dilatation of the ventricle after coronary occlusion. The trajectories of the nodes are shown in Fig. 16. Visually the nodes in the zone infarct show less motion.

IV. Discussion

Figure 17 shows that the velocity in the septum and in the lateral wall is influenced by the flow in the ventricle. These artifacts appear also in a large vertical stripe across the magnitude image as shown in Fig. 18.

These artifacts are due to the spatial misregistration of flowing blood. This represents the major limitation of the cine-phase velocity measurements. The strength of this algorithm (or the use of contour information in general) is to limit the impact on such corruptions to the data. Spatial presaturation pulses can reduce this signal slightly but it remains highly visible. Rapid imaging techniques such as Echo-Planar Imaging (EPI) could effectively freeze the motion of the blood and thus prevent these artifacts. In addition sequences producing black blood (absence of velocity in the ventricle) such as long TE spin echo EPI should make it possible to exploit the velocity information along the endocardium.

Another related problem stems from the difficulty of consistently defining the contour of the LV. The motion of the epicardium in the baseline study (pre-infarct) shows some erratic trajectories in the inferior wall (in Fig. 14,

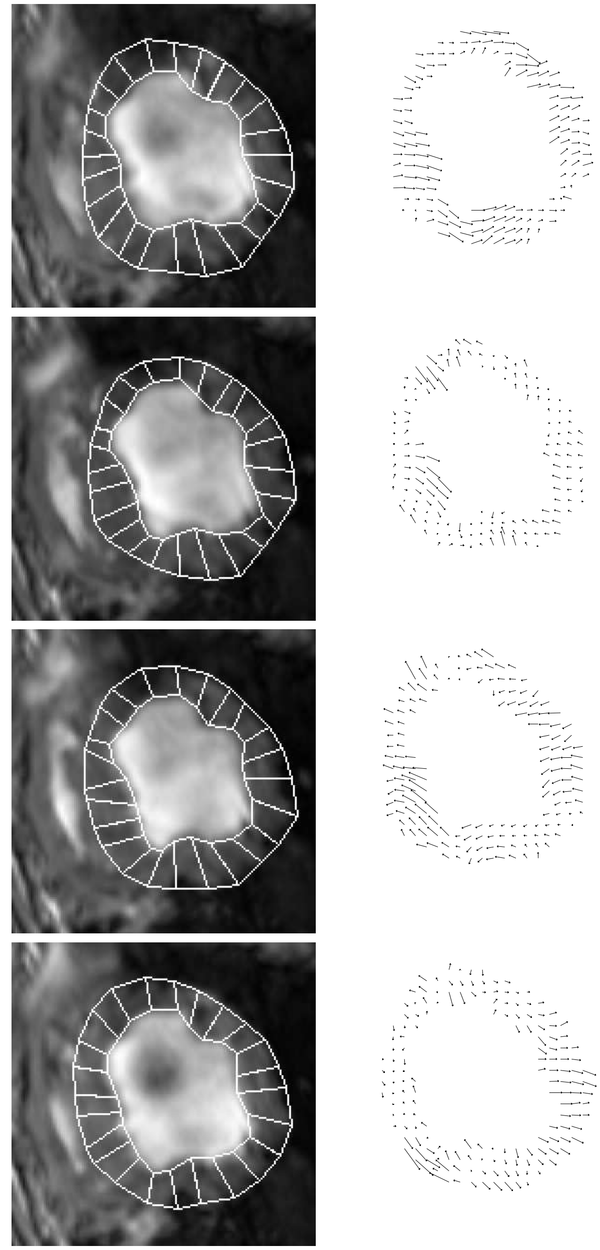

Fig. 15. *in vivo* study, post-infarct. Left: results of the tracking at time 1, 5, 9, and 14. Right: vector spline approximation of the velocity field at time 1, 5, 9, and 14. The tracking started at time 0 (end diastole)

this region corresponds to points (x, y) in the myocardium with $x \in [100, 140]$, and $y \in [140, 150]$). In theory the real motion of the epicardium should be small in this region. The apparent motion is due to an inconsistent detection of the contours. This problem is even more exemplified in the region around the left anterior descending artery (in Fig. 14, points (x, y) in the myocardium where $x \in [90, 110], y \in [90, 100]$). In this region, the contour of the LV is traced manually using a priori knowledge about the shape of the LV. However the same region has been inconsistently traced over the heart cycle, as shown in Fig. 13. As a result the tracking shows a large motion, even though the region should not undergo any significant

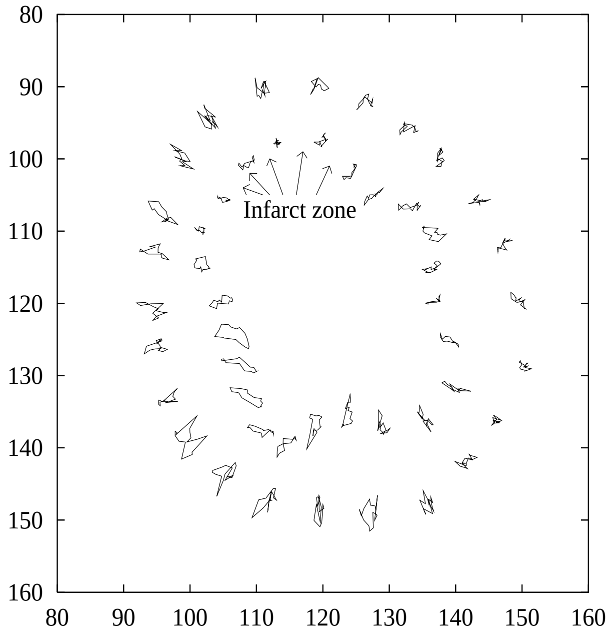

Fig. 16. *In vivo*, post-infarct, trajectories of the nodes. The arrows point toward the infarct zone. Visually the nodes in the zone infarct show less motion.

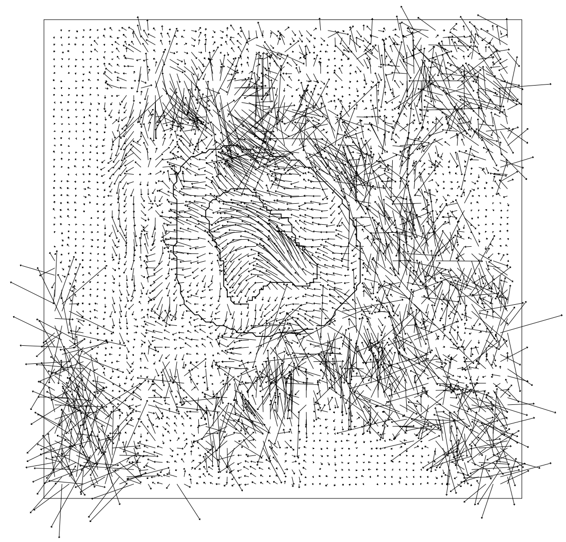

Fig. 17. Vector plot of the velocity field (u, v) at time = 9. The contours of the myocardium have been superimposed.

motion. Position measurements in the region have been weighted with a high covariance matrix, due to the absence of gradient. However, errors in the contour were systematic and not distributed randomly in time. They introduced a bias in the measurements. The contour detection algorithm could be improved by exploiting temporal coherence. Contours for instance could be detected as surfaces of spatiotemporal volumes.

We need to note that the trajectories presented in the *in vivo* experiment were obtained using a simplified 2-D problem. Only three contiguous slices have been collected ; only one was used. However the three-slice spatial resolution along the Z direction makes it possible to track in 3-D the middle slice. Indeed, even with significant out of plane motion, the slice will remain in the volume of data. In general an interpolation scheme will be necessary to combat the coarse resolution in the Z direction [20].

Our state model could be further improved by adding more harmonics. An interesting avenue of research consists in modeling the motion of the myocardium with a multiresolution approach. Gross motion could be described by low resolution terms, where local abnormalities could be characterized by higher order terms.

Another possible extension of the method concerns the use of shape information to calculate the position measurement. This would alleviate a possible shortcoming of the method: the correlation of the measurement with the prediction. In other words, the position measurement in the present algorithm relies too heavily on the accuracy of the prediction, and therefore on the accuracy of the model. In [31] we have exploited local curvature information to map the predicted mesh geometry with the contours extracted at the current instant. This scheme could be easily incorporated into our framework.

Finally, as explained in section III-A.1 it takes 2 to 3 time steps for the Kalman filter to reach its steady state mode. During this bootstrapping mode, the position estimate may be inaccurate. Because of the limited temporal resolution of the data this may be a limitation of our approach. An alternative method consists in using a global smoothing method that processes the 16 velocity fields, and the 16 contours all at once, instead of using an iterative approach. Unfortunately, this batch approach would be computationally intensive, whereas the computational load of the Kalman filter is quite light– and the filter can actually run in real time.

V. Conclusion

We have addressed the problem of the recovery of nonrigid motion from a sequence of velocity fields. We have proposed a new unified framework that exploits velocity fields and contour information to track the nonrigid motion of the LV. The method has been carefully evaluated with simulated data and phantom data. For the simulated data, the average error between the tracked nodes and the theoretical position was 1.8% of the total path length. The average error for the experiments with phantom data was 4.4% of the total path length. Thus, our unified framework for assessment of nonrigid myocardial motion, which integrates contour information with PC velocity maps, provides a reliable estimate of 2-D motion. This approach is being extended to 3-D.

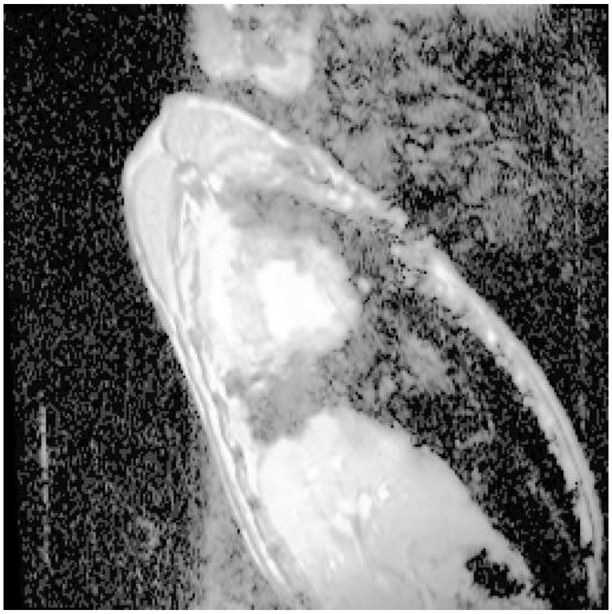

Fig. 18. Artifacts due to the spatial misregistration of flowing blood in the LV.

Acknowledgments

This work is supported in part by NIH Grant R01HL44803 from the National Heart, Lung and Blood Institute, by United States Air Force Grant F49620-93-1-0575, and by the Whitaker Foundation. The authors thank Amit Chakraborty for his help with the extraction of the contours of the LV, and Matthew Robson for his help in the design of the synthetic annulus sequences. The authors thank the reviewers for their comments and suggestions.

References

[1] N.J. Pelc, R.J. Herfkens, A. Shimakawa, and D. Enzmann. Phase contrast cine magnetic resonance imaging. *Magnetic Resonance Quaterly*, Vol.7, No 4:229–254, 1991.

[2] J.S. Duncan, R.L. Owen, L.H. Staib, and P. Anandan. Measurement of non-rigid motion using contour shape descriptors. In *Proc. Conference Computer Vision and Pattern Recognition, Hawaii*, pages 318–324, June 1991.

[3] A.A. Amini and J.S. Duncan. Bending and stretching models for LV wall motion analysis from curves and surfaces. *Image and Vision Computing*, 10 No 6:418–430, July/August 1992.

[4] P. Shi, A. Amini, G. Robinson, A. Sinusas, R.T. Constable, and J. Duncan. Shape-based 4-D left ventricular myocardial function analysis. In *Proc. IEEE Workshop on Biomedical Image Analysis, Seattle, Washington*, pages 88–97, 1994.

[5] L.K. Waldman. Multidimensional measurement of regional strains in the intact heart. In L. Glass, P. Hunter, and A. McCulloch, editors, *Theory of Heart*, Springer Verlag, 1991.

[6] M.A. Guttman, J.L. Prince, and E.R. McVeigh. Tag and contour detection in tagged MR images of the left ventricle. *IEEE Trans. on Medical Imaging*, Vol. 13, No.1:74–88, March 1994.

[7] C.C. Moore, W.G. O'Dell, E.R. McVeigh, and E.A. Zerhouni. Calculation of three-dimensional left ventricular strains from biplanar tagged MR images. *Journal of Magnetic Resonance Imaging*, 2:165–175, 1992.

[8] S. Kumar and D. Goldgof. Automatic tracking of SPAMM grid and the estimation of deformation parameters from cardiac images. *IEEE Trans. on Medical Imaging*, Vol. 13, No.1:122–132, March 1994.

[9] J.L. Prince and E.R. McVeigh. Motion estimation from tagged MR image sequences. *IEEE Trans. on Medical Imaging*, pages 238–249, June 1992.

[10] A.A. Young and L. Axel. Three-dimensional motion and deformation of the heart wall: Estimation with spatial modulation of magnetization-a model based approach. *Radiology*, 185:241–247, 1992.

[11] W.G. O'Dell, C.C. Moore, W.C. Hunter, E.A. Zerhouni, and E.R. McVeigh. Three-dimensional myocardial deformations: calculation with displacement field fitting to tagged MR images. *Radiology*, 195(3):165–175, 1995.

[12] A. Pentland and B. Horowitz. Recovery of non-rigid motion and structure. *IEEE Trans. on Pattern Analysis and Machine Intelligence*, pages pp 730–742, July 1991.

[13] A.A. Young and L. Axel. Non-rigid heart wall motion using MR tagging. In *Proc. Conference Computer Vision and Pattern Recognition*, pages 399–404, 1992.

[14] A.A. Young, D.L. Kraitchman, L. Dougherty, and L. Axel. Tracking and finite element analysis of stripe deformation in magnetic resonance tagging. *IEEE Trans. on Medical Imaging*, pages 413–421, Sept. 1995.

[15] D. Metaxas and D. Terzopoulos. Shape and nonrigid motion estimation through physic-based synthesis. *IEEE Trans. on Pattern Analysis and Machine Intelligence*, pages 580–591, June 1993.

[16] G.E. Mailloux, A. Bleau, M. Bertrand, and R. Petitclerc. Computer analysis of heart motion from two-dimensional echocardiograms. *IEEE Trans. on Biomedical Engineering*, Vol.34, No.5:356–364, May 1987.

[17] S.M. Song, R.M. Leahy, D.P. Boyd, B.H. Brundage, and S. Napel. Determining cardiac velocity fields and intraventicular pressure distribution from a sequence of ultrafast CT cardiac images. *IEEE Trans. on Medical Imaging*, 13:2:386–397, 1994.

[18] P. van Dijk. Direct cardiac NMR imaging of heart wall and blood flow velocity. *J. Comput. Assist. Tomogr.*, 8:429–436, 1984.

[19] R.T. Constable, K.M. Rath, A.J. Sinusas, and J.C. Gore. Development and evaluation of tracking algorithms for cardiac wall motion analysis using phase velocity MR imaging. *Magn. Reson. Med.*, Vol. 32:33–42, 1994.

[20] Y. Zhu, M. Drangova, and N.J. Pelc. Impact of spatial resolution and interpolation on myocardial tracking from cine PC data. In *Proc. of The Society of Magnetic Resonance, Third Meeting, Nice*, page 250, 1995.

[21] N.J. Pelc, M. Drangova, L.R. Pelc, Y. Zhu, D.C. Noll, B. Bowman, and R.J. Herfkens. Tracking of cyclic motion with phase-contrast cine MR velocity data. *J. Magn. Reson. Imaging*, Vol. 5:339–345, 1995.

[22] A. Lingamneni, P.A. Hardy, K.A. Powell, N.J. Pelc, and R.W. White. Validation of cine phase-contrast MR imaging for motion analysis. *J. Magn. Reson. Imaging*, Vol. 5:331–338, 1995.

[23] Y. Bar-Shalom and T.E. Fortmann. *Tracking and Data Association.* Academic Press, 1988.

[24] T.S. Denney and J.L. Prince. Reconstruction of 3-D left ventricular motion from plannar tagged cardiac MR images: An estimation approach. *IEEE Trans. on Medical Imaging*, pages 625–635, Dec. 1995.

[25] P.S.Maybeck. *Stochastic Models, Estimation and Control, Volumes 1 & 2.* Academic Press, 1982.

[26] R. Underwood and D. Firmin. *Magnetic Resonance of the Cardiovascular System.* Blackwell Scientific Publications, 1991.

[27] P.G. Walker, G.B. Cranney, M.B. Scheidegger, G. Waseleski, G.M. Pohost, and A.P. Yoganathan. Semiautomated method for noise reduction and background phase error correction in MR phase velocity data. *J. Magn. Reson. Imaging*, 3:521–530, 1993.

[28] A. Chakraborty, L.H. Staib, and J.S. Duncan. Deformable boundary finding influenced by region homogeneity. In *Proc. of Conference Computer Vision and Pattern Recognition, Seattle, Washington*, pages 624–627, 1994. To appear in IEEE TMI, 1996.

[29] C. de Boor. *A Practical Guide to Splines.* Springer-Verlag, 1978.

[30] J.M. Huyghe, T. Arts, D.H. Van Campen, and R.S. Reneman. Porous medium finite element model of the beating left ventricle. *American Journal of Physiology*, pages H1256–H1267, 1992.

[31] J.C. McEachen, F.G. Meyer, R.T. Constable, A. Nehorai, and J.S. Duncan. A recursive filter for phase velocity assisted shape-based tracking of cardiac motion. In *Proc. Fifth Int. Conf. on Comput. Vision, ICCV'95, Cambridge, MA*, pages 653–658, 1995.

[32] Y. Zhu, M. Drangova, and N.J. Pelc. Fourier tracking of myocardial motion using cine PC data. In *Proc. of The Society*

of Magnetic Resonance, Second Meeting, San Fransisco, page 1477, 1994.

[33] L. Ljung and T. Kailath. Backwards markovian models for second-order stochastic processes. *IEEE Trans. on Inform. Theory*, Vol. 22, no. 4:488–491, July 1987.

[34] G.S. Sidhu and U.B. Desai. New smoothing algorithms based on reversed-time lumped models. *IEEE Trans. on Automat. and Contr.*, Vol.21, no.4:538–541, Aug. 1976.

[35] M.A. Bernstein and Y. Ikezaki. Comparison of phase-difference and complex-difference processing in phase contrast MR angiography. *J. Magn. Reson. Imaging*, 1:725–729, June 1991.